

Made-To-Measure Models of Self-Similar Triaxial Halos with Steep Inner Density Gradients

J. C. Malvido,^{1*} J. A. Sellwood^{2†}

¹406 North Road, Chester, NJ 07930, US

²Rutgers University, Department of Physics & Astronomy, 136 Frelinghuysen Road, Piscataway, NJ 08854-8019, US

8 April 2019

ABSTRACT

We use the Made-to-Measure method to construct N -body realizations of self-similar, triaxial ellipsoidal halos having cosmologically realistic density profiles. Our implementation parallels previous work with a few numerical refinements, but we show that orbital averaging is an intrinsic feature of the force of change equation and argue that additional averaging or smoothing schemes are redundant. We present models having the Einasto radial mass profile that range from prolate to strongly triaxial. We use a least-squares polynomial fit to the expansion coefficients to obtain an analytical representation of the particle density from which we derive density contours and eccentricity profiles more efficiently than by the usual particle smoothing techniques. We show that our N -body realizations both retain their shape in unconstrained evolution and recover it after large amplitude perturbations.

Key words: methods: N-body simulations — methods: numerical — galaxies: halos — galaxies: kinematics and dynamics — galaxies: structure

1 INTRODUCTION

Dark-matter halos that form hierarchically in simulations of Λ CDM cosmology have a number of regular properties: Their mass density profiles, the distributions of velocity anisotropy, spin parameters, and substructure are largely independent of the halo’s mass over a wide range of values. Other properties, such as the concentration and triaxiality, vary systematically with halo mass (Zemp 2009; Diemand & Moore 2011; Frenk & White 2012).

The landmark work of Navarro et al. (1996, hereafter NFW) reported that the halo mass density could be fitted with a broken power-law

$$\rho(r) \propto \left(\frac{r}{r_s}\right)^{-\gamma} \left(1 + \frac{r}{r_s}\right)^{\gamma-3} \quad (1)$$

where the length scale, r_s , is the radius around which the logarithmic slope changes. The steepness of the inner cusp reflected in the value of the exponent γ has been the subject of much debate (Moore et al. 1999; Fukushige & Makino 2001; Power et al. 2003; Diemand et al. 2004, 2005). More recent work (Navarro et al. 2004, 2010; Merritt et al. 2005; Gao et al. 2008) finds the Einasto profile (described in §4) with its steep but finite central density to be a better fit.

Virialized halos that have undergone multiple mergers

acquire a triaxial shape in general, though with a strong bias towards prolateness (Frenk et al. 1988; Cole & Lacey 1996; Bailin & Steinmetz 2005). To accommodate triaxiality when fitting the mass density, a number of authors (Katz 1991; Dubinski & Carlberg 1991; Jing & Suto 2002, hereafter JS02) replace the radial coordinate r with the dimensionless coordinate $\tilde{\xi}$ defined through

$$\tilde{\xi}^2 = \frac{x^2}{a^2} + \frac{y^2}{b^2} + \frac{z^2}{c^2} \quad , \quad a \geq b \geq c \quad (2)$$

where a , b , and c are the lengths of the major, intermediate, and minor axes, respectively. Although axial ratios and alignments display some radial variation (JS02; Cole & Lacey 1996; Bailin & Steinmetz 2005; Schneider et al. 2012, hereafter SFC12), we focus here on creating self-similar ellipsoids for which these values remain in a fixed ratio, with the axes aligned, at all radii. This idealized geometry reduces the mass density to a function of a single variable $\tilde{\xi}$ (eq. 2), with the axis ratios b/a and c/a as constant parameters.

Self-similarity is an attractive assumption, but it is generally insufficient to enable a derivation of a distribution function (DF). The DF can be expressed in terms of the actions (Binney & Tremaine 2008), but these are known only in the case of the “perfect” ellipsoid for which the potential is fully separable in ellipsoidal coordinates (de Zeeuw & Lynden-Bell 1985; de Zeeuw 1985) and all orbits are regular. Regular orbits also exist in more general

* E-mail: jmalvido@verizon.net

† E-mail: sellwood@rutgers.edu

ellipsoids but irregular orbits, for which the only isolating integral is the energy, populate some parts of phase space, and may even dominate (Udry & Pfenniger 1988; Valluri & Merritt 1998; Valluri et al. 2010).

Various approaches have been adopted to construct N -body models of triaxial mass distributions with some success. Holley-Bockelmann et al. (2001) and Widrow (2008) “squeeze” a spherical model, Rodionov et al. (2006, 2009) developed an iterative method that corrects the density after each time step, without revising the velocities, until equilibrium is attained, while Moore et al. (2004) construct them through multiple collisions of separate systems. However, neither the squeeze nor collision methods provide a systematic means for reproducing a specific geometry, such as self-similarity, while only halos with a central core, rather than a steep inner density gradient, have been attempted with the iterative method.

Schwarzschild (1979, 1993) built triaxial models from linear combinations of bound orbits in the desired potential. In his method, orbits are drawn from a pre-calculated library that approximately spans the phase-space of the bound system and contains the time-averaged contributions to the mass density in a set of spatial cells. The assignment of orbital weights is constrained by the targeted mass density in these cells, but since the assignment is far from unique, it is customary to seek an optimal solution, such as by maximizing the entropy (Richstone & Tremaine 1988) to favor a smooth distribution. The method has been successfully applied to cuspy, triaxial systems (Merritt & Fridman 1996; Merritt 1997; Capuzzo-Dolcetta et al. 2007; van de Ven et al. 2008; Vasiliev & Athanassoula 2012). However, creation of N -body models requires the further, non-trivial step of selecting particles from appropriately chosen points along the orbits selected from the library.

Here we adopt the “made to measure” (hereafter M2M) algorithm proposed by Syer & Tremaine (1996, hereafter ST96), which is similar in spirit to Schwarzschild’s but adjusts the mass of each moving particle dynamically. The algorithm has been further developed by De Lorenzi et al. (2007, hereafter DL07), Dehnen (2009, hereafter D09), Long & Mao (2010), Morganti & Gerhart (2012), and Hunt & Kawata (2013), and a useful brief review is given by Gerhard (2010). A further advantage of M2M is that, on completion, the equilibrium N -body system is ready to use with no additional step. The range of applications of M2M (De Lorenzi et al. 2008, 2009; Das et al. 2011; Long & Mao 2012; Long et al. 2013) is a fair measure of its versatility.

One can add observational constraints to both M2M (DL07) and Schwarzschild’s method (see e.g. Chanamé et al. 2008, and references therein) in order to construct models for comparison with data, which is probably the most widely used application of these methods. But our objective in this paper is purely theoretical.

Our aim is to use M2M to construct N -body realizations of self-similar ellipsoidal halos with a mass density and eccentricity suggested by cosmological simulations. While an improvement on spherical halos, our models are still idealizations, since cosmological halos are generally not self-similar, and we also neglect rotation (e.g. Bullock et al. 2001), certain kinematic features (Cole & Lacey 1996; Wojtak et al.

2005; Hansen 2009) and substructure (Diemand et al. 2004, 2005; Springel et al. 2008).

Some triaxial models have already been created by this technique, notably in DL07 and D09, but there are minor differences in our approach and we present more extensive tests of the stability of the resulting models. We will use them in later work to study the influence of halo triaxiality on the dynamics of embedded disks.

2 THE ALGORITHM

The M2M method has already been described elsewhere (e.g., ST96, DL07, D09). We therefore give only an outline, noting where our treatment differs from previous work. Our presentation follows closely that given by DL07, but we do not require their generalization to include constraints from velocity data.

2.1 Preliminaries

We seek to create equilibrium halo models with a target density distribution $\rho_T(\mathbf{x})$ and total mass \mathcal{M}_T in the gravitational potential $\Phi_T(\mathbf{x})$. In most applications, the potential arises from the density ρ_T only, but it is also possible to consider models with additional mass components, such as a disk or central mass, that contribute to Φ_T but not to ρ_T .

First we divide the volume of the target model into a set of K cells, each having a volume \mathcal{V}_k , and define a set of occupancy kernels $\{\mathcal{K}_k(\mathbf{x}), k = 1, \dots, K\}$

$$\mathcal{K}_k(\mathbf{x}) = \begin{cases} 1 & \mathbf{x} \text{ is within } \mathcal{V}_k \\ 0 & \text{otherwise.} \end{cases} \quad (3)$$

The mass in the k th cell is therefore given by

$$P_k = \int \mathcal{K}_k(\mathbf{x}) \rho_T(\mathbf{x}) d^3\mathbf{x}. \quad (4)$$

Suppose that we were to construct a trial set of particles (e.g., as described in §3.7)

$$\mathcal{F}_0(\mathbf{z}) = m_p \sum_{i=1}^N w_{0i} \delta(\mathbf{z} - \mathbf{z}_i(t=0)), \quad (5)$$

where $\mathbf{z} = (\mathbf{x}, \mathbf{v})$ is a 6D phase space coordinate. The initial density is determined by the adopted set of N particle position coordinates $\{\mathbf{x}_i(0)\}$ with their initial fractional weights $\{w_{0i}\}$ normalized by the fiducial particle mass m_p (see §3.4) such that $m_p \sum_{i=1}^N w_{0i} = \mathcal{M}_T$. At $t = 0$, this initial guess therefore has the mass in each of K cells

$$p_{0k} = m_p \sum_{i=1}^N w_{0i} \mathcal{K}_k(\mathbf{x}_i(0)). \quad (6)$$

The density at later times, $\rho(\mathbf{x}, t)$, is determined by integrating all particle trajectories to time t in the frozen potential Φ_T , when the mass in each cell becomes

$$p_k(t) = m_p \sum_{i=1}^N w_i(t) \mathcal{K}_k(\mathbf{x}_i(t)). \quad (7)$$

Schwarzschild’s approach is first to compute the time average occupancy of each particle in each cell

$$\mathcal{K}_{ik} \equiv \frac{1}{\tau} \int_0^\tau \mathcal{K}_k(\mathbf{x}_i(t)) dt, \quad (8)$$

for some large but finite time period τ , and then to require that

$$\langle p_k \rangle = m_p \sum_{i=1}^N w_i \mathcal{K}_{ik} = P_k, \quad (9)$$

for a set of time-independent and non-negative $\{w_i\}$. Since the space of possible solutions to eq. (9) is generally large, it is desirable to optimize for smoothness; a popular choice is to maximize the ‘‘entropy’’, which is defined as

$$S = -\frac{1}{N} \sum_{i=1}^N w_i \ln \left[\frac{w_i}{\tilde{w}_i} \right]. \quad (10)$$

We use our initially guessed weights for the priors, i.e. $\tilde{w}_i = w_{0i}$, but other choices are possible. An entropy decrease, $\Delta S < 0$, may be interpreted as an increase of ‘‘order’’ in the physical system; for example, a sphere is less ordered than an ellipsoid.

2.2 Made to measure

In the M2M method, the particle weights $w_i(t)$ are adjusted, while maintaining the condition $\rho(\mathbf{x}, t) \approx \rho_T(\mathbf{x})$, as the particle trajectories are integrated. It is usually cast as an optimization problem in which the ‘‘likelihood function’’

$$\mathcal{L}(t) = \mu S(t) - \mathcal{C}(t), \quad \text{with } \mu > 0 \quad (11)$$

is to be maximized. Both parts of this objective are time-dependent, since the weights are adjusted. The ‘‘cost function’’ is

$$\mathcal{C}(t) = \frac{1}{2} \sum_{k=1}^K \left[\frac{p_k(t) - P_k}{\hat{\sigma}_k} \right]^2, \quad (12)$$

where $\hat{\sigma}_k$ is the dispersion of p_{0k} , i.e., the sampling uncertainty implicit in generating $\mathcal{F}_0(\mathbf{z})$ (DL07, D09).

The condition for the optimal solution for $\{w_i^*\}$ when $w_i^* \geq 0$ is (Avrieli 1976)

$$w_i^* \frac{\partial \mathcal{L}}{\partial w_i} = 0. \quad i = 1, \dots, N \quad (13)$$

Therefore, either $w_i^* = 0$, or

$$\frac{\partial \mathcal{L}}{\partial w_i} = \mu \frac{\partial S}{\partial w_i} - \frac{1}{N} \sum_{k=1}^K \frac{\mathcal{K}_k(\mathbf{x}_i)}{\hat{\sigma}_k} \Delta_k = 0, \quad (14)$$

where $\Delta_k \equiv (p_k - P_k)/\hat{\sigma}_k$.

2.3 The FOCE

Originally proposed by ST96, the force-of-change-equation (FOCE)

$$\dot{w}_i = \epsilon w_i \frac{\partial \mathcal{L}}{\partial w_i}, \quad (15)$$

with ϵ being a small parameter, provides a rule for adjusting w_i in order to drive $\partial \mathcal{L}/\partial w_i$ towards zero, a procedure in a simulation that is readily combined with the particle motion.

The $w_i(t)$ and $\Delta_k(t)$ functions have noisy paths owing to N -body sampling noise and the movement of particles

across cells, which causes abrupt changes to the values of $\mathcal{K}_k(\mathbf{x}_i)$. ST96 suggested replacing the Δ_k in eq. (15) with its *moving average*, $\tilde{\Delta}_k$, such that $\tilde{\Delta}_k(0) = \Delta_k(0)$ and

$$\frac{d\tilde{\Delta}_k}{dt} = \eta (\Delta_k - \tilde{\Delta}_k) \quad (16)$$

where $\eta \geq 2\epsilon$, as a means of suppressing large fluctuations in the FOCE from these sources of noise and likened its effect to that of smearing a set of virtual particles over a given orbit. This adjustment has been integral to implementations of M2M reported in the literature. D09 points out, however, that this procedure is inconsistent with the extremum condition (13) and compromises the meaning of \mathcal{C} in eq. (12) since the $\hat{\sigma}_k$ reflect the original N -body shot noise, not the reduced noise. Instead, D09 applies a moving average to $\partial \mathcal{L}/\partial w_i$, and, in combination with eq. (15), obtains a second order ODE for $\ln w_i$.

However, the following argument suggests that such attempts at explicit averaging are redundant. Formally, the FOCE may be integrated to give

$$w_i(t) = e^{\epsilon D_i(t)} w_{i0}, \quad (17)$$

where

$$D_i(t) \equiv \int_0^t \frac{\partial \mathcal{L}}{\partial w_i} dt'. \quad (18)$$

Thus we see that $\epsilon D_i(t)$ is proportional to the time average $\langle \partial \mathcal{L}/\partial w_i \rangle_t$. Substitution of eq. (14) for the integrand in (18) shows that the behavior of $\epsilon D_i(t)$ is dominated by orbital averages of the form $\langle \mathcal{K}_k(\mathbf{x}_i) \Delta_k \rangle_t$. But $\mathcal{K}_k(\mathbf{x}_i)$ is influenced by the trajectory of the i th particle only, while Δ_k is determined by all particles in the k th cell. If the number of such particles is sufficiently large, it is reasonable to expect that $\langle \mathcal{K}_k(\mathbf{x}_i) \Delta_k \rangle_t$ decouples at large times into the product of two independent averages $\mathcal{K}_{ik} \times \langle \Delta_k \rangle_t$, where \mathcal{K}_{ik} is defined in eq. (8). Furthermore, ST96 and DL07 prove that $\langle \Delta_k \rangle_t \rightarrow 0$ at large times which, from the definition of Δ_k , implies $\langle p_k \rangle_t \rightarrow P_k$. Thus we effectively recover eq. (9) and thereby formally establish the asymptotic equivalence of the M2M and Schwarzschild’s methods.

Therefore, not only is explicit averaging redundant but the application of eq. (16) is counterproductive if N is large enough. We have not explored how large N needs to be for this statement to be true, but when we employ $N = 1.2 \times 10^6$ particles, we find that inclusion of the averaging procedure (16) degrades the actual value of \mathcal{C} by as much as an order of magnitude. We therefore refrain from including any additional averaging.

Thus we find a deeper resemblance between the M2M approach and Schwarzschild’s method. However, there are two reasons for preferring M2M: not only does eq. (14) combine averaging and solving for $\{w_i^*\}$ into a single algorithm instead of two distinct steps but, upon convergence, it also delivers a representative set of particle coordinates that are in equilibrium, in readiness for an N -body simulation.

2.4 Convergence

Fluctuations in the values of the $w_i(t)$ as the system evolves jointly with the FOCE imply that satisfying condition (13) for all N particles simultaneously at any given instance is implausible. Instead, an equally effective, yet more realistic,

goal of the M2M method is to ensure that $\max \|\langle \Delta_k \rangle\| < \delta$, for some prescribed threshold δ .

By linearizing the FOCE (exclusive of the entropy term), ST96 (see also DL07) obtained a set of equations for the modes of the $\langle \Delta_k \rangle$ and demonstrated that these modes decay exponentially – a result that essentially formalizes the intuition behind the intent of the FOCE. Though it does not provide practical guidelines for assessing convergence, it does, however, render the $\langle \Delta_k \rangle$, rather than the $w_i(t)$, as the focus of the convergence analysis.

The threshold, δ , may be made as small as desired by reducing μ , with the disadvantage that an increasing number of particle weights are driven toward zero. Reaching a desired threshold δ is not necessarily indicative of convergence; only when changes in the entropy become small relative to its level can the algorithm be said to have reached convergent conditions.

Ultimately, the true test of the algorithm's convergence is whether the resulting system maintains the desired shape and mass profile as it evolves freely and *self-consistently* without intervention from the FOCE (see §5.2).

2.5 Summary of the Procedure

Our implementation of the algorithm, which will be discussed in greater detail later, may be conveniently summarized as follows (see also D09):

(i) *Initialization*: Construct an equilibrium, spherically symmetric model with the desired mass density profile consisting of N_M particles. Transform the particle coordinates by rescaling (see eq. 21 below) to achieve the targeted geometry and adjust the velocities so that the tensor virial theorem is satisfied.

(ii) *Relaxation*: Allow the system to settle (without the FOCE) for 20 – 25 dynamical times.

(iii) *M2M step*: Evolve the system while adjusting the weights in accordance to the FOCE.

(iv) *Convergence check*: Once the entropy level is nearly constant, switch off the FOCE and allow the system to evolve self-consistently to test whether it is in equilibrium.

(v) *Stability Check*: Apply an adiabatic, aspherical perturbation to seed any possible secular instabilities and follow the subsequent self-consistent evolution.

Note that we obtain a smooth target potential Φ_T and the values of $\hat{\sigma}_k$ needed for steps (ii) and (iii) by creating a model having many more particles than is practical to evolve, i.e., $N_T \gg N_M$. Their positions, with velocities ignored, give a smoother representation of ρ_T , and we can solve for their gravitational field using our adopted N -body method.

It is possible to run M2M using a self-consistent, rather than a rigid, potential. This is less satisfactory, however, because M2M continuously tries to adjust weights to compensate for (mild) particle scattering. We therefore prefer to use a smooth and frozen target potential.

3 COMPUTATIONAL METHODS

3.1 Self-Similar Ellipsoid

The target triaxial halos in this work consist of a series of concentric and co-eccentric, nested ellipsoidal shells - a sim-

plifying idealization. Surfaces of constant density in a self-similar ellipsoid have constant ξ , where

$$\xi^2 = x^2 + y^2 \frac{a^2}{b^2} + z^2 \frac{a^2}{c^2}. \quad (19)$$

Here a , b , and c are the semi-axes of the outer surface of the finite ellipsoid. We also define the eccentricities, $\varepsilon_y = (1 - b^2/a^2)^{1/2}$ and $\varepsilon_z = (1 - c^2/a^2)^{1/2}$ for later use. Strongly triaxial systems have values of the triaxiality parameter, $\mathbf{T} \equiv (\mathbf{a}^2 - \mathbf{b}^2)/(\mathbf{a}^2 - \mathbf{c}^2) \sim 0.5$, while $T = 0$ for an oblate, and $T = 1$ for a prolate, spheroid.

We wish to construct self-similar ellipsoids for which the density profile $\rho_e(\xi)$ has the same functional form (to within a normalization factor to preserve the same total mass) as some spherical model $\rho_s(r)$. We relate a point $\mathbf{r} = (x, y, z)$ on a sphere to $\mathbf{r}' = (x', y', z')$ on the ellipsoidal surface through $r^2 = x^2 + y^2 + z^2 = x'^2 + y'^2 a^2/b^2 + z'^2 a^2/c^2 = \xi^2$,

which is equivalent to the scale transformation

$$x' = x \quad ; \quad y' = ya/b \quad ; \quad z' = za/c. \quad (21)$$

Two ellipsoidal surfaces at ξ and $\xi + \delta\xi$ bound a volume known as a *thin homoeoid* (BT08, §2.5). The volume of a thin homoeoid is $4\pi\theta_{yz}\xi^2 d\xi$, with $\theta_{yz} \equiv bc/a^2$, while that of a spherical shell is $4\pi r^2 dr$. Therefore, if a sphere of radius a and density $\rho_s(r)$ is compressed along the intermediate and minor axes by factors b/a and c/a respectively in such a way that equidensity shells do not cross, it yields a self-similar ellipsoid of equal mass with density $\rho_e(\mathbf{x}) = \theta_{yz}^{-1} \rho_s(\xi)$.

3.2 Force computation

Particle-mesh, or grid, methods remain the most efficient for N -body simulations of an isolated gravitating system (Sellwood 2014). Here we use a radial grid that computes forces from an expansion in surface harmonics on a set of spherical shells that are more closely spaced near the center. An arbitrary field function $\Psi(\mathbf{x})$ (e.g., the gravitational potential, force components, mass density, etc.) can be written in real form as

$$\Psi(\mathbf{x}) = \sum_{l=0}^{\infty} \sum_{m=0}^l \gamma_{lm} \Pi_l^m(\theta) [\Psi_{lm}^c(r) \cos m\phi + \Psi_{lm}^s(r) \sin m\phi], \quad (22)$$

where $\mathbf{x} = (r, \theta, \phi)$ is the field point,

$$\Pi_l^m(\theta) \equiv \sqrt{\frac{(l-m)!}{(l+m)!}} P_l^m(\cos \theta), \quad (23)$$

$P_l^m(\cos \theta)$ is the associated Legendre function, and the normalization factor $\gamma_{lm} = (2 - \delta_{m0})(2l+1)/4\pi$. The coefficients in eq. (22) can be computed from

$$\begin{pmatrix} \Psi_{lm}^c(r) \\ \Psi_{lm}^s(r) \end{pmatrix} = \int \Pi_l^m(\theta') \begin{pmatrix} \cos m\phi' \\ \sin m\phi' \end{pmatrix} \Psi(r, \theta', \phi') \sin \theta' d\theta' d\phi'. \quad (24)$$

Truncating the expansion (22) at some $l = l_{\max}$ smooths small-scale angular fluctuations.

We employ the N -body scheme described by Sellwood (2003) that uses a 1D grid for the radial coordinate while retaining the exact angular expansion for each particle. The radial nodes are spaced logarithmically,

and subdivide a spherical volume into shells of gradually increasing thickness. The functions Ψ_{lm}^α are tabulated at shell boundaries and evaluated at other radii by linear interpolation. To ensure radial continuity, individual particle masses are divided between neighboring grid points according to the cloud-in-cell procedure, which also distinguishes between mass interior and exterior to a field point. The particles are smeared in angle because the expansion (22) is limited by the adopted l_{\max} . The end result may be pictured as each point particle being replaced by a smeared density distribution wedged between neighboring spherical radial shells. See Sellwood (2003) or <http://www.physics.rutgers.edu/~sellwood/manual.pdf> for a full description.

3.3 M2M Binning

A particle within the k th radial shell, which spans the range (r_{k-1}, r_k) , contributes to $(l_{\max} + 2)(l_{\max} + 1)$ real terms $\Psi_{lm}^\alpha(r_k)$. If we were to use the gravity grid shells to define the cells in eq. (3) as in DL07, then $n_r + 1$ radial nodes would yield a total of $n_r(l_{\max} + 2)(l_{\max} + 1)$ separate kernel moments $\mathcal{K}_{k;lm}^\alpha$ (eq. 28); note that each particle contributes to a single radial shell k and to multiple (l, m, α) components.

Since n_r typically ranges in the hundreds, we superimpose a coarser grid – the M2M grid – consisting of $k_r + 1 \ll n_r$ nodes, where all nodes in the M2M grid coincide with nodes of the finer gravity grid. Coarser radial spacing not only reduces the particle shot noise in each bin but also improves the efficiency in solving the FOCE by reducing the number of kernel moments to be computed.

It may seem that one of these grids is superfluous, for if the resolution of the M2M grid is adequate to resolve the mass density, then it should be adequate to resolve the gravitational forces. However, as argued above, the FOCE averages over a large number of particle trajectories making coarser M2M binning acceptable, while the finer gravity-grid is needed to resolve forces and determine accurate particle trajectories.

3.4 Unequal particle masses

Even though they are less closely spaced than the gravity nodes, the M2M grid spacings should still be small, especially in the inner half of the halo, in order to represent the targeted shape. But with equal mass particles, fine binning causes larger statistical fluctuations in the cell occupancy. We therefore employ particles that are less massive near the center and have gradually increasing masses towards the outer edge. To achieve this, we use the dimensionless function $W(L) = L_0 + L$ to weight the *initial* particle masses. Here, L ($\equiv |\mathbf{L}|$) is the specific angular momentum (in our dimensionless units, see §4.3) and L_0 a convenient constant. To maintain the desired initial density, we select particles from the DF weighted by $W^{-1}(L)$ to ensure that lighter particles are proportionately more numerous (Sellwood 2008).

We store the initial value $w_{i0} = W(L_i)$ for each particle, which we subsequently adjust during M2M as required by the FOCE (eq. 15). Furthermore, we adopt the initial weights w_{i0} for the priors \tilde{w}_i in the entropy term (10).

Since $\mathcal{M}_T = \int \int f d^3\mathbf{v} d^3\mathbf{x}$, the fiducial particle mass

$$m_p = \frac{1}{N} \int \int \frac{f}{W} d^3\mathbf{v} d^3\mathbf{x}, \quad (25)$$

so that the actual mass of each particle is m_p times its current weight $w_i(t)$, and $m_p \sum_i w_{i0} \equiv \mathcal{M}_T$.

3.5 Target Moments and Kernel Computation

Estimates of the local density from a system of N particles are notoriously noisy, so we work with integrated masses. As in DL07, we define the (l, m, α) *mass harmonic* component in the k th bin of the M2M grid as

$$M_{k;lm}^\alpha = \int_{r_{k-1}}^{r_k} r^2 \rho_{lm}^\alpha(r) dr, \quad (26)$$

where values of $\rho_{lm}^\alpha(r)$ are derived from eq. (24) with $\Psi(\mathbf{x})$ replaced by $\rho_T(\mathbf{x})$.

Applying eq. (26) to a discrete particle density yields the corresponding harmonic mass components $m_{k;lm}^\alpha$ due to particles

$$\begin{pmatrix} m_{k;lm}^c \\ m_{k;lm}^s \end{pmatrix} = m_p \sum_{i,k}^N w_i \Pi_l^m(\theta_i) \begin{pmatrix} \cos m\phi_i \\ \sin m\phi_i \end{pmatrix}, \quad (27)$$

where m_p is given by eq. (25). Similarly, the kernel $\mathcal{K}_k(\mathbf{x}_i)$ in eq. (3) is given by

$$\begin{pmatrix} \mathcal{K}_{k;lm}^c(\mathbf{x}_i) \\ \mathcal{K}_{k;lm}^s(\mathbf{x}_i) \end{pmatrix} = \begin{cases} m_p \Pi_l^m(\theta_i) \begin{pmatrix} \cos m\phi_i \\ \sin m\phi_i \end{pmatrix} & \mathbf{x}_i \text{ in bin } k \\ 0 & \text{otherwise.} \end{cases} \quad (28)$$

For the FOCE, the deviation becomes

$$\Delta_{k;lm}^\alpha = \frac{m_{k;lm}^\alpha - M_{k;lm}^\alpha}{\sigma_{k;lm}^\alpha}. \quad (29)$$

§3.9 describes how we estimate the denominator $\sigma_{k;lm}^\alpha$.

3.6 The FOCE

We use a forward difference to integrate the FOCE, a first order ODE. The parameter ϵ determines the rate of change of \dot{w}_i , which is also driven by contributions from all other particles in the same radial bin. By iterating multiple n_F times at fixed t with the adjusted constant ϵ/n_F until the solution of the FOCE is well converged, we improve the overall convergence properties of the algorithm and diminish the fluctuations in Δ_k . After each intermediate iteration, we update the right side of the FOCE and renormalize to preserve the total mass $m_p \sum_i w_i(t)$.

DL07 suggest the value of ϵ should be a small parameter, ϵ_0 , times $[\max_{i,k} |\mathcal{K}_k(i) \Delta_k / \sigma_k|]^{-1}$. We adopt their suggestion, but since the maximum value is subject to large swings, especially at the outset, we limit its time variability by employing a moving average.

3.7 Halo Initialization

Our method to prepare the model for M2M integration is similar to that described by D09, whereas DL07 employ the squeeze method to obtain the initial equilibrium, triaxial figure. We proceed as follows:

(i) Determine the DF for a spherically symmetric, isotropic halo of density $\rho_s(r)$ by Eddington inversion, and then redefine the DF to be zero for $E > E_{\max}$, where $E_{\max} = \Phi(r_{\max})$, with $r_{\max} = a$, the semi-major axis of the target ellipsoid. The density tapers smoothly to zero at r_{\max} , even though the truncation in E is sharp. We apply the weighting scheme described in §3.4 and select N_M particles in the usual way (Sellwood & Debattista 2009, §2.3). This procedure yields a self-consistent spherical model that is close to equilibrium; the change in central attraction near the outer edge caused by the tapered density creates only a very mild imbalance.

(ii) Apply the scaling transformation, eq. (21), to the spatial coordinates of the particle phase-space generated in step (i) in order to deform the sphere onto a self-similar ellipsoid, without changing the particle velocities.

(iii) Evaluate the potential energy W_{ij} and kinetic energy K_{ij} tensor components using the *frozen* gravitational field of the target ellipsoid (determined as described below) and velocities from the spherical equilibrium model, respectively, and rotate the phase-space coordinates slightly so that the kinetic and potential energy tensors become rigorously diagonal. We also adjust the velocity components of each particle so that on average $W_{ii}/2K_{ii} = 1$ for all three Cartesian components.

(iv) Evolve the system for 25 dynamical times, defined in §4.3 below, in the fixed gravitational field of the target ellipsoid to allow for relaxation during which the model becomes slightly less flattened.

3.8 M2M grid

In determining the nodes of the M2M grid, we use the spherical radii of the N_M particles generated in step (i) above to ensure that each radial bin initially contains at least a preset number of particles, or extends over a maximum prescribed number of gravity grid nodes, whichever criterion yields the fewer nodes. Thus, bins near the center where the density is high have the radial extent of only a few gravity grid nodes, while bins are as large as we allow in lower density regions.

3.9 Target Ellipsoid

To construct a *target potential* that is as smooth as possible, we duplicate steps (i) and (ii) of the above halo initialization procedure for a system of N_T particles, with $N_T \gg N_M$. The target potential is that of the larger number of particles, which suffers from milder shot noise.

Moreover, we draw multiple, independent samples of N_M particles each from the N_T target population in order to estimate the mean target moments, $\bar{M}_{k,lm}^\alpha$, and associated dispersions, $\sigma_{k,lm}^\alpha$ (eq. 29), based on the statistical spreads of the samples.

4 AN EXAMPLE: THE EINASTO HALO

4.1 Mass Density

Navarro et al. (2004, 2010), Merritt et al. (2005, 2006), and Gao et al. (2008) show that the logarithmic slope of the

Label	$(\varepsilon_y, \varepsilon_z)$	Axis Ratios	Triaxiality
T _A	(0.60,0.80)	(0.80,0.60)	0.563
T _B	(0.70,0.80)	(0.71,0.60)	0.766
P	(0.80,0.80)	(0.60,0.60)	1.000

Table 1. Axis ratios and triaxiality parameters of our three Einasto halo models.

spherically-averaged mass density in well-resolved cosmological halos can be fitted as a power law, $d \ln \rho(r)/d \ln r = -2(r/r_s)^\kappa$, with the value of κ dependent on the mass of the halo. The scale r_s is the radius at which the logarithmic slope = -2 . The density that has this property is the Einasto profile (Einasto & Haud 1989)

$$\rho_E(r) = \frac{M_0}{16\pi r_s^3} \exp \left\{ -\frac{2}{\kappa} \left[\left(\frac{r}{r_s} \right)^\kappa - 1 \right] \right\}, \quad (30)$$

which rises steeply towards the center, but remains finite. Cardone et al. (2005) give formulas for the mass, potential, and force in terms of the incomplete gamma function $\gamma(p, x)$ and its complement $\Gamma(p, x)$, which is distinguished from the usual Gamma function $\Gamma(x)$ by the number of arguments. The mass profile is

$$M_E(r) = M_0 \left(\frac{\kappa}{2} \right)^{3/\kappa} \frac{e^{2/\kappa}}{4\kappa} \gamma \left[\frac{3}{\kappa}, \frac{2}{\kappa} \left(\frac{r}{r_s} \right)^\kappa \right], \quad (31)$$

which yields a total mass

$$M_E(\infty) = M_0 \left(\frac{\kappa}{2} \right)^{3/\kappa} \frac{e^{2/\kappa}}{4\kappa} \Gamma \left(\frac{3}{\kappa} \right), \quad (32)$$

and a gravitational potential

$$\Phi_E(r) = -\frac{GM_E(\infty)}{r_s \Gamma \left(\frac{3}{\kappa} \right)} \left\{ \frac{\gamma \left[\frac{3}{\kappa}, \frac{2}{\kappa} \left(\frac{r}{r_s} \right)^\kappa \right]}{r/r_s} + \frac{\Gamma \left[\frac{3}{\kappa}, \frac{2}{\kappa} \left(\frac{r}{r_s} \right)^\kappa \right]}{(\kappa/2)^{1/\kappa}} \right\}. \quad (33)$$

We adopt this profile for our spherical mass model, fixing $\kappa = 0.17$, which is the value Navarro et al. (2004) preferred for their three prototype galaxy groups and highest resolution haloes (Navarro et al. 2010).

We set $r_{\max} = 15$, so that the total mass of our models is $1.497M_0$. (Note $M_E(r_{\max}) = 1.960$ using eq. (31); the difference is due to energy truncation that tapers the density smoothly to zero at r_{\max} .) We select particles with individual masses using $L_0 = 0.1$ (see §3.4) which causes $\sim 95\%$ of all particles to lie within $r = 8$, a radius we label as $r_{0.95}$.

From the discussion in §3.1, the density of our Einasto *ellipsoid* is

$$\rho_e(\mathbf{x}) = \theta_{yz}^{-1} \rho_E(\xi), \quad (34)$$

which obviously reduces to $\rho_E(r)$ for $\varepsilon_y = \varepsilon_z = 0$.

4.2 Three models

Three ellipsoidal halo models summarized in Table 1 are the focus of this work. All have Einasto index $\kappa = 0.17$, a semi-major axis truncated at $r_{\max} = 15r_s$, and are strongly flattened ($c/a = 0.6$) along the minor axis, but differ in their intermediate axes. Although their triaxiality parameters, which are typical of cosmologically formed halos (JS02, SFC12), increase from model T_A to P, model T_A is the most strongly triaxial.

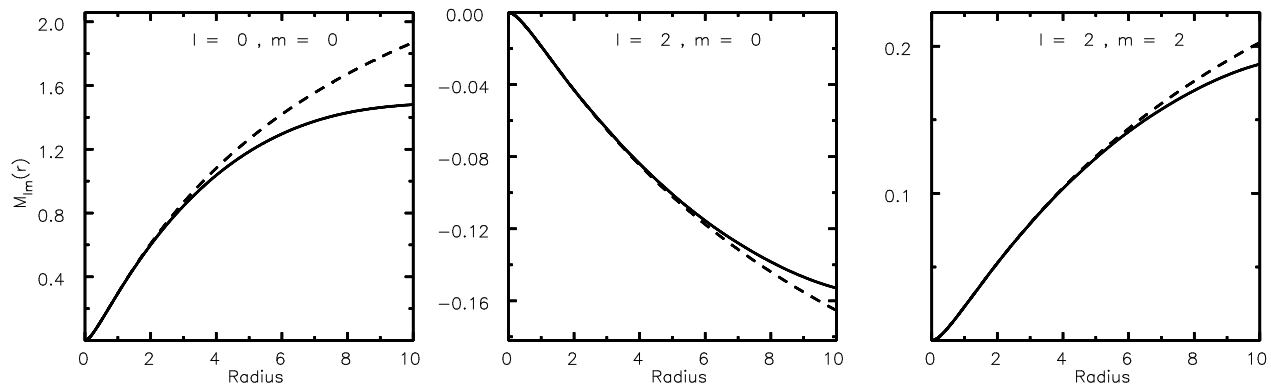


Figure 1. The solid curves show the target mass harmonic profiles up to $l = 2$ for model P. The dashed curves show the corresponding profiles of an ellipsoid of density given by eq. (34) without an energy cut off.

	Aq	SmP	T _A	T _B	P
r_s (kpc)	20.3	20.0	20.0	20.0	20.0
r_{200} (kpc)	177.3	232.0	209.9	210.1	210.1
r_{\max} (kpc)	39.5	31.3	33.4	31.7	30.7
v_{\max} (km s ⁻¹)	203.2	216.3	206.2	210.1	215.7
c_{200}	8.7	11.6	10.5	10.5	10.5
$\mu_{200} (\times 10^{11})$	12.95	13.48	9.97	10.0	10.0

Table 2. Rotation curve characteristics of halo models. Aq refers to halo model Aq-D-2 in Navarro et al. (2010). The column marked SmP refers to the smooth ellipsoid ρ_e with the eccentricities of the P model

Ellipsoids have reflection symmetry about their three principal planes. We therefore align our coordinate x -axis with the major axis and the z -axis with the polar axis in order that only the even terms of the surface harmonic expansion are non-zero. Oriented in this manner, the $m = 0$ components of the $l/2 \geq 1$ harmonics characterize the eccentricity along the minor axis, while even $m \geq 0$ terms describe the density along the intermediate axis. We retain even l terms up to $l_{\max} = 4$ only.

Fig. 1 illustrates the profiles of the three main contributions – monopole and quadrupole moments – for model P and compares the $M_{lm}^c(r)$, $l \leq 2$, computed from the smooth density ρ_e , with those for $\bar{M}_{lm}^c(r)$ for the target ellipsoid.

4.3 Units

We employ natural units, for which $r_s = M_0 = G = 1$, throughout. The unit of velocity is therefore $v_{\text{dyn}} \equiv (GM/r_s)^{1/2}$ and the dynamical time is $\tau_{\text{dyn}} \equiv (r_s^3/GM)^{1/2} = r_s/v_{\text{dyn}}$.

We compare our models with the cosmologically-simulated halo model Aq-D-2 extracted from Navarro et al. (2010, their Tables 1 and 2), which also has the Einasto index ($\kappa = 0.17$). Fig. 2 shows rotation curves computed from the spherically averaged mass, $v_{\text{rot}}(r) = [\bar{M}_{00}^c(r)/r]^{1/2}$ from which we deduce the peak circular v_{\max} and virial v_{200} velocities. Setting the length scale to $r_s = 20$ kpc, close to that of Aq-D-2, and $\tau_{\text{dyn}} = 50$ Myr, we have $M = 6.74 \times 10^{11} M_{\odot}$ and velocity unit $v_{\text{dyn}} \simeq 391$ km s⁻¹. The figure highlights the impact of spherically averaging the target density on otherwise identical models of different eccentricities.

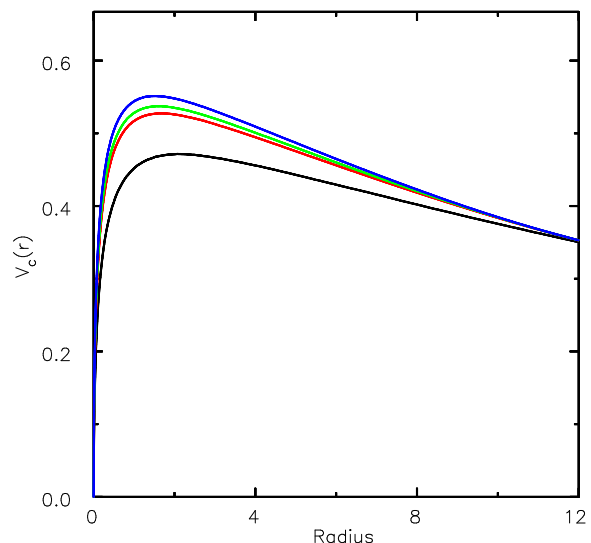


Figure 2. Spherically averaged rotation curves $V_c(r) = [G\bar{M}_{00}^c(r)/r]^{1/2}$ (in natural units) for each model. The lower curve (black) is that of the underlying spherical halo, while increasing the triaxiality parameter yields higher velocity peaks: T_A (red), T_B (green), and P (blue).

4.4 Implementation

Each of the halo models in Table 1 to be simulated in an M2M run consists of $N_M = 1.2 \times 10^6$ particles, while their associated target models – from which we derive the target potential, moments and dispersions – have $N_T = 4.5 \times 10^7$ particles.

With the parameter $L_0 = 0.1$, we find $\sim 2.5 \times 10^5$ particles inside a radius $r = 0.1$ (first 16 grid nodes) for the simulation models. To obtain a specific M2M binning scheme, we sample N_M particles from the target population then identify aggregations of gravity grid nodes with a minimum of 2.5×10^5 particles or a maximum of 10 such nodes, except near the center where strict adherence to the criterion makes the first few bins too wide: we shorten the first bin to 5 nodes, which contains between 6000 to 8000 particles; conversely, at the boundary we widen the last occupied bin to 20 to 30 nodes so that it contains $\gtrsim 1000$ particles. This particular scheme typically yields a maximum of 60 M2M radial

bins (56 of which are occupied initially) to encompass the 501 gravity-grid nodes. In cases where a given target value $\bar{M}_{k,lm}^\alpha$ vanishes due to symmetry, sampling typically yields a nonzero mean with a dispersion that greatly exceeds the mean; we omit the corresponding $\Delta_{k;lm}^\alpha$ when solving the FOCE to further improve efficiency.

Step (ii) in §3.7 achieves the ellipsoidal arrangement, and (iii) a phase-space near equilibrium. The velocity adjustments in the last step yield a mild radial anisotropy, β (BT08, see also §5.3) that gradually increases from $\gtrsim 0$ (isotropy) at the origin to a maximum near the boundary as the triaxiality parameter increases, i.e., $\beta \sim 0.1$ for model T_A, while $\beta \sim 0.3$ for model P.

We compute accelerations from the rigid target potential during the M2M evolution, and advance the motion of all particles using leapfrog with a time step $\Delta t = 0.0025$. After each time step, we solve the FOCE using a fixed minimum number n_F of iterations, gradually increasing n_F (from $n_F = 5$ initially to a maximum of 12) so that at the end of the M2M evolution $|\Delta_{k;lm}^\alpha| < 0.1$ on average. To achieve this threshold we choose $\mu = 0.5$ and $\varepsilon_0 = 0.005$. Although the entropy in the P and T_B models converges sooner, we still iterate all models for 200 dynamical times, in order to allow particles in the outer halo envelope to complete more than one full orbit and to enable most off-grid particles to return. Only a negligible number remains permanently outside the grid, as reported below (Table 4).

After the end of the M2M evolution, we continue the evolution for a further 100 dynamical times with a fully self-consistent simulation. This continued evolution enables us to check the long term survival of the shape imposed by the M2M technique. We also increase l_{\max} to 6, to better capture the strong flattening along the polar axis, and include odd- l ($< l_{\max}$) contributions to the force determination, as further tests of the robustness of the shape.

5 RESULTS

Tables 3 and 4 summarize the range of values of key M2M quantities for our three models near or at completion of the procedure. Since the behavior of the M2M objective, \mathcal{L} , is essentially stochastic, Table 3 gives the best and worst values of the objective to which we add the associated entropy \mathcal{S} , cost function \mathcal{C} and bin threshold, $\max |\Delta_{k;lm}^\alpha|$.

The more strongly elongated models have greater order, a trend that is reflected in $\Delta S(\infty)$. To support this interpretation, we reran a version of model T_A – model T_{A2} – for which we omitted steps (ii) and (iii) of the initialization, i.e., used a spherically symmetric halo, but otherwise used the same parameters and procedure during the M2M evolution as for the T_A model. The resulting entropy converges to the lower value -0.80 ; hence, nearly 40% of the prospective change in the entropy is captured through the direct distortion of the spherical model in our initialization process.

Table 4 gives the percentage of off-grid particles and of particles that have been driven to a zero weight, $N_0(\infty)$. These are but a tiny fraction of N_M . The percentage of massless particles that lie within the radii $r_{0.95}$, $N_0(r_{0.95})$, and $r_{0.95}/2$, $N_0(r_{0.95}/2)$, at the end of the M2M evolution indicates that most massless particles are near the outer edge.

	T _A		T _B		P	
	B	W	B	W	B	W
Objective (\mathcal{L})	-0.39	-0.52	-0.43	-0.75	-0.45	-0.64
Chi-square (\mathcal{C})	0.27	0.53	0.32	0.96	0.31	0.68
Entropy ($\Delta\mathcal{S}$)	-0.52	-0.52	-0.54	-0.54	-0.59	-0.59
$\max \Delta_{k;lm}^\alpha $	0.08	0.14	0.09	0.16	0.07	0.13

Table 3. Best (B) and worst (W) M2M objective near completion of algorithm. Other quantities associated with the same instances.

	T _A	T _B	P
Off-grid	0.002	0.005	0.025
$N_0(\infty)$	0.033	0.075	0.097
$N_0(r_{0.95})$	0.012	0.025	0.035
$N_0(r_{0.95}/2)$	0.005	0.009	0.014

Table 4. Percent of off-grid and zero-weighted particles at the end of the M2M evolution.

The increase in the numbers of massless particles with the triaxiality parameter is strongly correlated with the lower (greater) entropy change (ordering), whereas the off-grid particle count, which also appears to be correlated with triaxiality, is actually driven by the initialization method. Thus, there are *no* off-grid particles for model T_{A2}, supporting the earlier observation of the effect of initialization steps (ii) and (iii) as tending to generate highly eccentric outer orbits. In this case also $N_0(\infty) \sim 0.18\%$ – i.e., there are five times as many zero mass particles as in T_A.

Fig. 3 shows the radial variation of $\bar{M}_{lm}(r)$, or target profiles, and $m_{lm}(r)$, derived from the particles, for model P. The curves are drawn to $r = 10$, which contains $> 98\%$ of the particles and at two times: the end of both the M2M and self-consistent runs; their close agreement in the inner halo gives an indication of how well the desired shape is achieved.

For a more quantitative measure, we give values of the *cumulative relative error*, $\delta_{lm} \equiv |m_{lm}(r_{0.95}) - \bar{M}_{lm}(r_{0.95})|/|\bar{M}_{lm}(r_{0.95})|$ in Table 5 for the principal (l, m) contributions explicitly included in the M2M algorithm. Not surprisingly, the relative errors are smallest for the monopole terms, which are numerically the largest. Since all three halos are equally strongly flattened, the smallest errors are for the ($l, 0$) components, while the errors for the ($l, m > 0$) components decrease with increasing triaxiality parameter, a relationship that is reinforced in the prolate model P. This trend can also be understood in terms of the sampling uncertainty due to the relative contributions from the higher harmonics: decreasing the triaxiality parameter at fixed flattening decreases the contribution of the $m > 0$ harmonics and increases the associated sampling uncertainty relative to the $m = 0$ harmonics. Note that for the self-consistent runs, the smaller error in the $m > 0$ components as triaxiality parameter increases follows from the same reasoning.

5.1 Testing Self-Similarity

Katz (1991), JS02 and Debattista et al. (2008) analyze the shapes of their halos directly from the particles by fitting an ellipsoid over iteratively refined particle volumes, while SFC12 diagonalizes the local inertia tensor.

We avoid these numerically costly techniques and in-

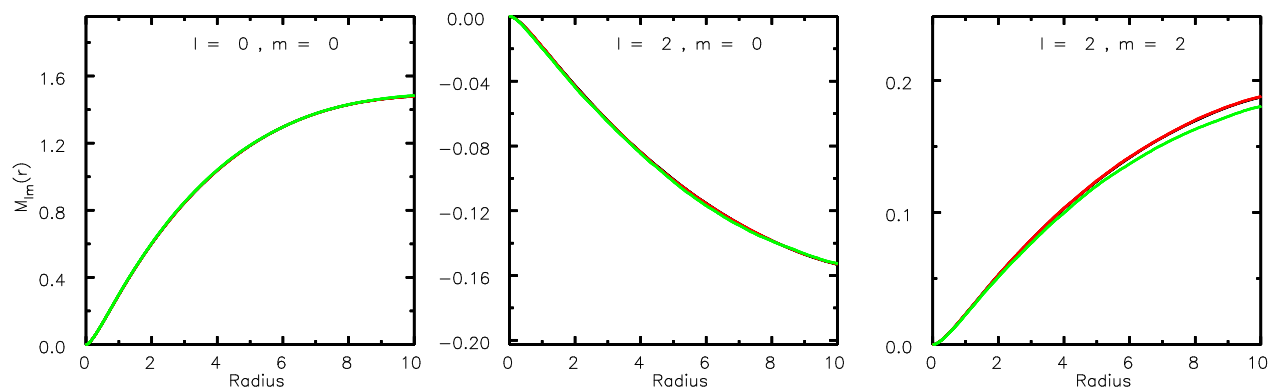


Figure 3. Target (black), M2M (red) and self-consistent (green) mass harmonic cosine curves of the model P. The black curves are barely visible due to the excellent agreement of the red curves.

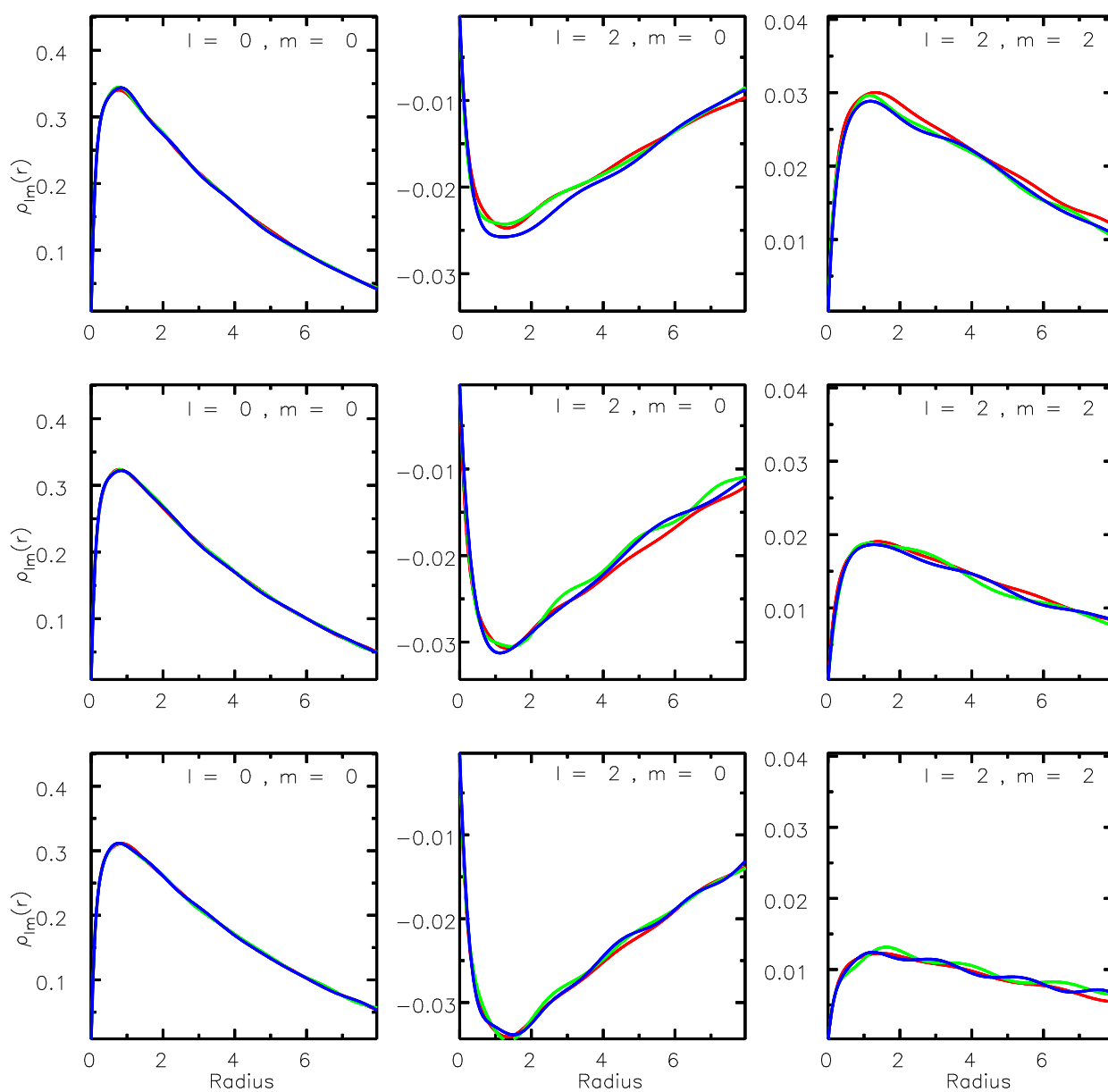


Figure 4. Monopole and quadrupole density moments of P (top row), T_B (middle row), and T_A (bottom row) models. Curves displayed are at the ends of the M2M (red), self-consistent (green) and perturbed (blue) phases.

(l, m)	T_A		T_B		P	
	M2M	SC	M2M	SC	M2M	SC
(0, 0)	-3.94	-2.76	-3.53	-2.87	-3.50	-3.15
(2, 0)	-4.43	-1.95	-3.11	-2.39	-3.08	-2.72
(2, 2)	-2.27	-1.25	-2.40	-1.39	-2.48	-1.42
(4, 0)	-1.66	-1.31	-1.56	-1.35	-1.47	-1.74
(4, 2)	-2.46	-0.61	-2.57	-0.89	-3.01	-1.02
(4, 4)	-1.56	-0.19	-1.56	-0.94	-1.89	-1.45

Table 5. Log_{10} of cumulative error δ_{lm} of the mass harmonics at end of both M2M and self-consistent (SC) runs.

stead use a least-squares fit with Chebyshev polynomials of the values of $m_{lm}^\alpha(r_k)$ at each node k of the gravity grid, but require the value of the fit and its derivative to vanish at the origin. Differentiation of the fitted function, $\mu_{lm}^\alpha(r)$, yields the corresponding weighted-densities, $r^2\rho_{lm}^\alpha(r)$, shown in Fig. 4. These components are combined as in eq. (22) to yield an approximate expansion for the total density

$$\rho(\mathbf{r}) \approx \sum_{l=0}^{l_{\max}} \sum_{m=0}^l \gamma_{lm} \Pi_l^m(\theta) [\cos m\phi \rho_{lm}^c(r) + \sin m\phi \rho_{lm}^s(r)], \quad (35)$$

where $\rho_{lm}^\alpha(r) = r^{-2} d\mu_{lm}^\alpha/dr$.

Eq. (35) forms the basis for testing self-similarity. We examine both the radial eccentricity profiles and planar equidensity contours of our halo models by fitting ellipses to the contours with the least-squares algorithm of Bender & Möllenhof (1977), a procedure that allows eccentricity, orientation and centering to be estimated simultaneously. The left-hand column of Fig. 5 shows the eccentricity profile of the primary models, while the middle and right-most columns show, respectively, the density contours on the XY - and ZX -planes. Table 6 gives the eccentricity values at a fixed set of points along the major axis evaluated at the ends of both the M2M and unconstrained evolution. Of particular interest are those of the self-consistent runs as they correspond to freely evolving, equilibrium halos. Except for mild deviations in the outer halo, the tabulated values show remarkable uniformity along a given principal axis. It is noteworthy that the magnitude of these deviations decreases with increasing eccentricity. Thus, while the eccentricity along the minor axis is very stable for all three models ($< 3\%$ error), along the largest departures ($\sim 5\%$) on the intermediate axis arise in the model with the least eccentricity. The centers of all computed ellipses differ by no more than a part in 10^3 , while the direction of the major axis fluctuates by less than 2° , declining outwards, with no systematic difference caused by the unconstrained evolution.

In order to compute projected surface densities, we note that eq. (19) can be rewritten as $\xi^2 = \tilde{q}^2 + z^2/(1 - \varepsilon_z^2)$. Thus a projection along the z -axis yields a surface density $\sigma(\tilde{q})$. For a projection onto the XY -plane, we integrate along the polar axis to obtain a surface density expansion

$$\Sigma(R, \varphi) = \sum_{m=0}^{l_{\max}} [\Sigma_m^c(R) \cos m\varphi + \Sigma_m^s(R) \sin m\varphi] \quad (36)$$

such that

$$\Sigma_m^\alpha(R) = \sum_{l=m}^{l_{\max}} \gamma_{lm} \int_{-\infty}^{\infty} dz \Pi_l^m\left(\frac{z}{r}\right) \rho_{lm}^\alpha(r), \quad (37)$$

where $r = (R^2 + z^2)^{1/2}$. Table 7 gives computed eccentricities for all three models for the self-consistent runs. To perform a similar projection along a different axis, particle coordinates are first rotated so that the axis of projection becomes the new polar axis, then apply the above equations.

5.2 Stability

If there were any *linearly* unstable modes present in our models, they would be seeded by shot noise. But all three models retain close to a constant eccentricity and axial alignment in their interior over 100 dynamical times of self-consistent evolution, hence any such modes must have negligible growth rates.

To test for *nonlinear* stability, we conduct an additional simulation in which we introduce into each of our halo models a perturber that is turned on adiabatically over a 50 dynamical times period and turned off over the same time period; we refer to these as perturbed runs. We try these experiments on the models at the end of the respective self-consistent run. Our adopted perturbation is the $l = 2$ density components of an Einasto ellipsoid with the same scale, same dimension and same α -parameter as the host halo, but only 10% of the mass and different eccentricities. We use a perturber with $(\varepsilon_y, \varepsilon_z) = (0.55, 0.85)$ for the T_A model, $(0.65, 0.85)$ for T_B , and $(0.75, 0.85)$ for P (see May & Binney 1986, for a similar concept), and our experiments terminate after 100 dynamical times. In figs. 4 and 5, the corresponding results for perturbed runs are shown in blue. Some quantitative differences are evident: model P is no longer perfectly prolate and deviations from the target self-similar profile are $< 10\%$ very near the center. Nevertheless, the figures remain qualitatively unchanged and may be therefore deemed as highly stable.

5.3 Anisotropy

We compute the spherically-averaged anisotropy parameter $\beta(r) = 1 - [\sigma_\theta^2(r) + \sigma_\varphi^2(r)]/2\sigma_r^2(r)$ (BT08) over the range $0 < r \leq r_{0.95}$. Here, $\sigma_\theta^2(r)$, $\sigma_\varphi^2(r)$ and $\sigma_r^2(r)$ are respectively the variances of the polar, azimuthal, and radial velocities.

Fig. 6 shows anisotropy profiles for our three principal models at the end of their respective self-consistent runs, but also includes four other models with lower triaxiality parameters for comparison. These are a sphere (S), an oblate spheroid (O) with $\varepsilon_z = 0.8$, and two low triaxiality ellipsoids with $(\varepsilon_y, \varepsilon_z) = (0.3, 0.8)$ (T_C) and $(0.45, 0.8)$ (T_D). These additional models were created in the same manner as our principal models through the self-consistent runs, but for the sphere we fit only the monopole component during the M2M run and admit $l_{max} = 2$ for the self-consistent evolution. Fig. 6 confirms that the sphere has $\beta \approx 0$ as expected, especially in the well-resolved interior region. The tangential bias ($\beta < 0$) near the boundary is an artifact of enforcing the targeted monopole moments in that region; the same effect can be seen in the oblate and triaxial models T_C and T_D . Flattening causes a radial bias ($\beta > 0$) in the inner regions, which is enhanced in the mildly triaxial models, gradually

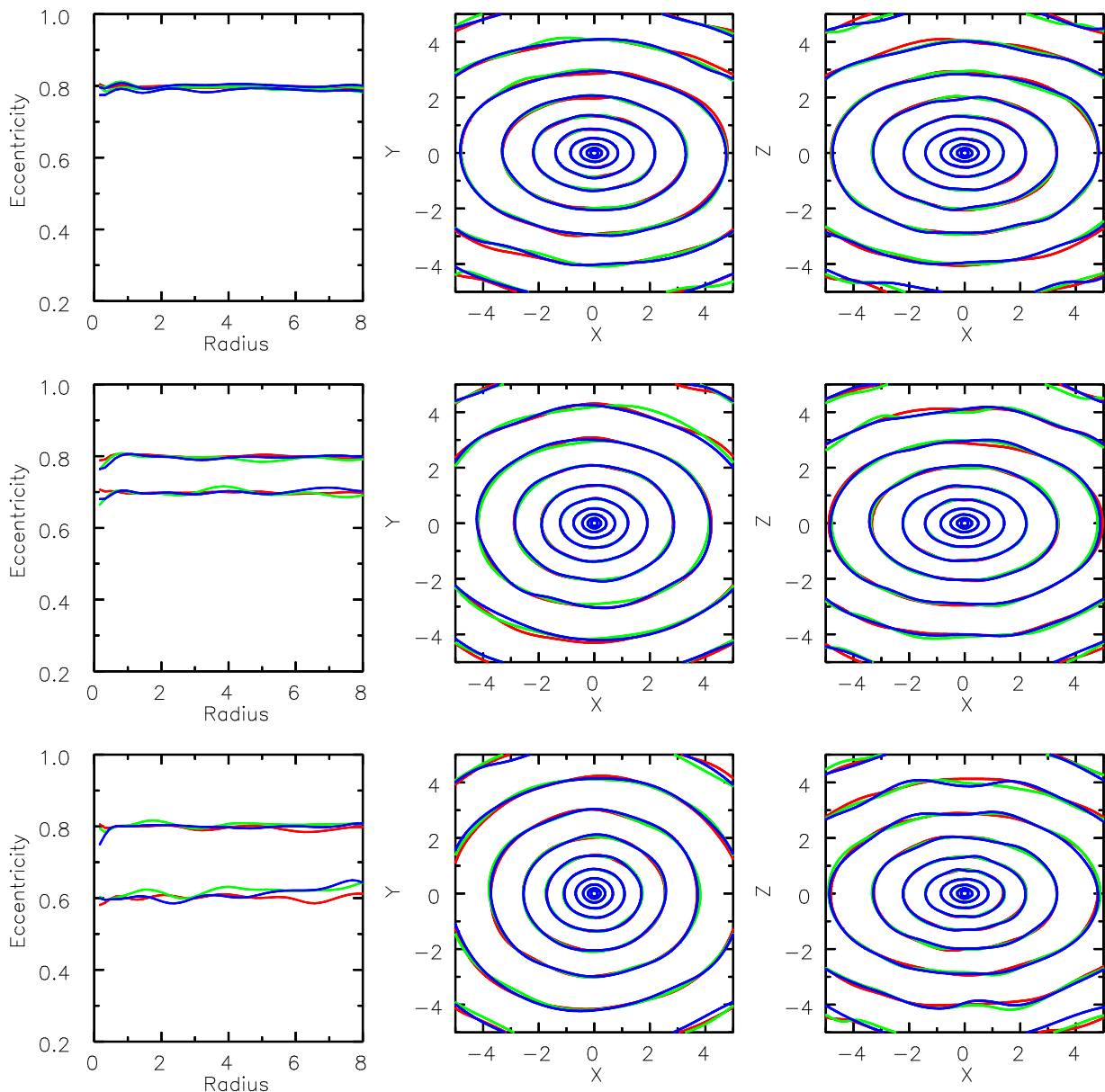


Figure 5. The left panels show the eccentricity profiles derived from least-squares ellipse fits to P (top), T_B (middle), and T_A (bottom) models. The middle and right panels of each row show density contours on the XY- and XZ-planes, respectively. The colours in all panels refer to the ends of the M2M (red), self-consistent (green) and perturbed (blue) evolution.

overcoming the tangential bias at the boundary. Indeed, the fiducial models, which have the highest triaxialities, are radially biased throughout.

The thick black lines in the same figure are adapted from the middle panel of Fig. 3 of Ludlow et al. (2011), which consists of halos in the Millennium-II simulation with Einasto parameter $\alpha = 0.178$. The broken black line shows the median anisotropy profile of their halo sample, while the thick black lines represent the upper and lower bounds of an envelope that encloses the bulk of the plotted profiles. Profiles for our fiducial models all lie within the envelope, while those of the added models with low triaxiality either straddle or lie beneath the lower boundary, a result consistent with the high triaxiality, prolate bias exhibited by cosmological halos (SFC12). Thus, even as an idealization, the self-similar

triaxial geometry is supported by an anisotropy profile indistinguishable from that of cosmological halos with comparable triaxiality, a noteworthy result given that we have not constrained the velocities in our models.

5.4 Run time

In keeping with the averaging property of the FOCE (see §2.3), every particle ought to complete several orbits to ensure convergence. Periods of orbits with radius near and beyond r_{200} of Einasto halos easily exceed 100 dynamical times so strict adherence to such a criterion would require excessively long running times. However, a more reasonable length of M2M evolution achieves robust self-similarity in the halo's interior while self-similarity in the outer region

x	T_A				T_B				P			
	$\varepsilon_y = 0.60$		$\varepsilon_z = 0.80$		$\varepsilon_y = 0.70$		$\varepsilon_z = 0.80$		$\varepsilon_y = 0.80$		$\varepsilon_z = 0.80$	
	M2M	SC										
0.10	0.585	0.613	0.816	0.809	0.703	0.700	0.798	0.791	0.811	0.808	0.816	0.806
0.15	0.581	0.604	0.808	0.798	0.698	0.694	0.791	0.784	0.803	0.798	0.807	0.800
0.25	0.583	0.596	0.799	0.786	0.695	0.689	0.791	0.779	0.796	0.788	0.799	0.795
0.50	0.599	0.598	0.796	0.793	0.702	0.698	0.803	0.790	0.796	0.789	0.798	0.804
0.75	0.603	0.602	0.800	0.801	0.703	0.704	0.805	0.800	0.800	0.796	0.801	0.812
1.00	0.599	0.607	0.801	0.803	0.700	0.702	0.802	0.802	0.799	0.795	0.800	0.808
2.00	0.606	0.613	0.803	0.814	0.696	0.698	0.800	0.798	0.799	0.797	0.799	0.792
3.00	0.599	0.602	0.790	0.794	0.698	0.698	0.799	0.794	0.798	0.796	0.794	0.796
4.00	0.608	0.629	0.797	0.807	0.701	0.714	0.798	0.800	0.799	0.798	0.796	0.801
5.00	0.599	0.621	0.800	0.807	0.701	0.700	0.801	0.786	0.798	0.793	0.798	0.797
6.00	0.597	0.618	0.786	0.804	0.693	0.691	0.799	0.787	0.799	0.790	0.799	0.792

Table 6. Eccentricity profiles at ends of the M2M and self-consistent (SC) evolution.

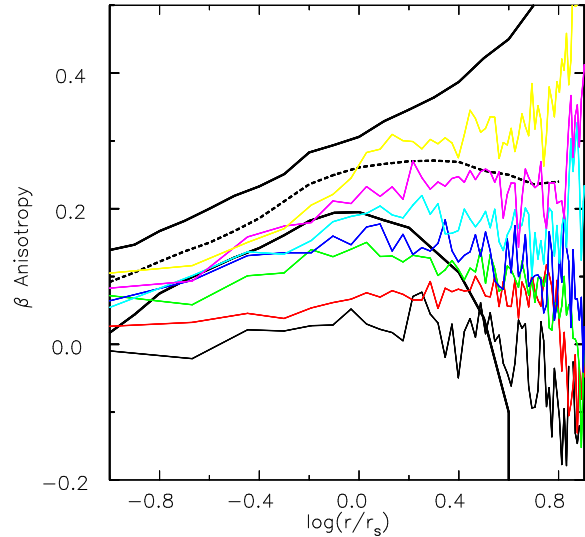
x	T_A	T_B	P
	$\varepsilon_y = 0.60$	$\varepsilon_y = 0.70$	$\varepsilon_y = 0.80$
0.10	0.618	0.678	0.807
0.15	0.601	0.674	0.795
0.25	0.582	0.679	0.783
0.50	0.567	0.701	0.788
0.75	0.572	0.707	0.794
1.00	0.591	0.703	0.793
2.00	0.611	0.699	0.787
3.00	0.600	0.696	0.786
4.00	0.612	0.688	0.796
5.00	0.611	0.680	0.790
6.00	0.614	0.687	0.790

Table 7. Profiles of the eccentricity of the surface density projected onto the XY-plane at end of the self-consistent runs.

of the halo remains less than perfect. This is illustrated in Fig. 7 which displays the quadrupole densities $\rho_{20}(r)$ (right) and $\rho_{22}(r)$ (center), and the eccentricity profile (left) after running times of 100 (red), 150 (green), 200 (blue) and 250 (cyan) dynamical times and the subsequent self-consistent run for the T_A model. We have omitted the monopole density ρ_{00} since all three cases align perfectly with the targeted density, which suggests it is the first moment to fully converge. It is evident that the ρ_{20} moment converges sooner than ρ_{22} , especially near the boundary, which is reflected in the eccentricity profile. We have verified that model P has converged adequately by 150 dynamical times. Table 5 underscores the connection between accuracy of fitting the various moments, high eccentricity and its reduction in the uncertainty of the moment due to particle noise. In our implementation, more eccentric models converge more rapidly.

6 SUMMARY AND CONCLUSIONS

We have used the M2M method to create collisionless halo models with self-similar, ellipsoidal geometry and a mass density profile relevant to cosmological halos. Our model halos are self-similar, which is not in strict accord with cosmological results (JS02, SFC12), but is a reasonable approximation with theoretically advantageous properties. They are the first step in an ongoing study of the collisionless growth of stellar disks within triaxial halos.

**Figure 6.** Anisotropy profiles arranged in ascending triaxiality parameter: Spherical (thin black line), Oblate (red), T_D (green), T_C (blue), T_B (cyan), T_A (magenta), and P (yellow) halo models (see text for definition of non-fiducial models). Superimposed on these are the upper and lower boundaries (thick black lines) of the profiles in Fig. 3 of Ludlow et al. (2011) and the corresponding median curve (broken black line).

Both DL07 and D09 have previously created triaxial halos by this method, but there are minor differences in our approach, and we have adopted a more cosmologically motivated model. The main difference in methodology is that we do not implement a moving average, (eq. 16), which we find actually degrades the results and we show why it is superfluous. Other minor differences in our approach are described in §4.4.

DL07 introduced the M2M objective as a goodness-of-fit measure to accommodate observational data. Our present application is to a theoretical target model, and we highlight the similarities and differences between M2M and Schwarzschild's approach. We also follow DL07 and D09 by interpreting the dispersions as sampling error consistent with shot noise inherent in any N -body representation, but construct our target potential from a static N -body model with a very large number of particles, which we use not only

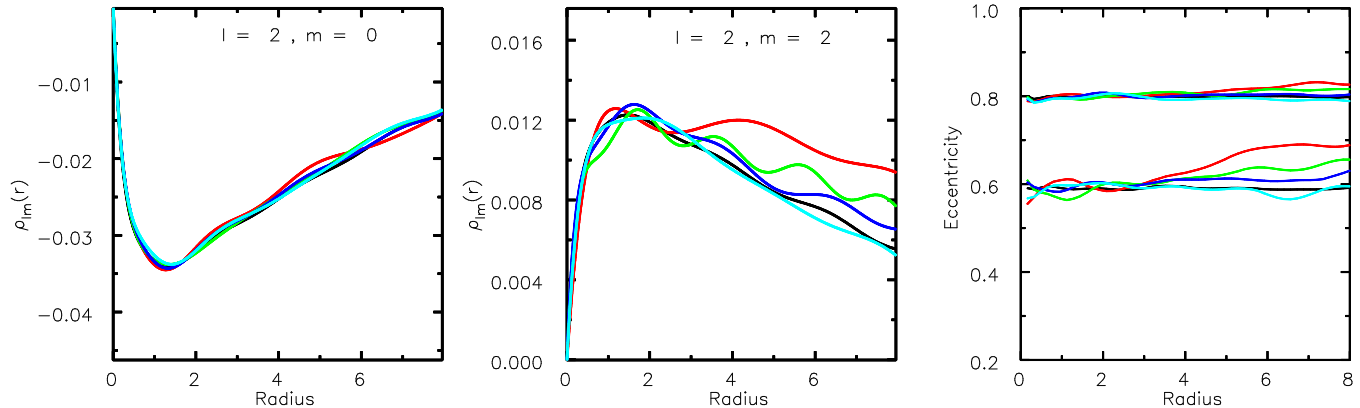


Figure 7. Quadrupole weighted densities $m = 0$ (left), $m = 2$ (center) and eccentricity profile of the T_A model for target (black) and M2M run times of 100 (red), 150 (green), 200 (blue) and 250 dynamical times (cyan) shown after respective self-consistent runs.

to compute the target potential, but also to determine the mean and dispersions that serve as proxies for P_j and σ_j , respectively, in eq. (12).

The full procedure consists of several distinct steps: after initializing the particles as described in §3.7, we allow the model to relax in the smooth target potential for 25 dynamical times. We then apply the FOCE over 200 dynamical times, a sufficient time span to ensure that changes in the entropy level are minimal.

Our adopted model is the Einasto halo and we present three aspherical models that bear strong similarities to halos from the Millenium-II simulation selected by Ludlow et al. (2011). We demonstrate that they are stable by evolving them in their self-consistent potential over a period of 100 dynamical times, during which their properties barely changed. We also tested non-linear stability by perturbing the model and showed that its shape was restored quite well after the perturbation was removed. In additional experiments, not presented here, we have found that singular mass profiles, such as the NFW or Hernquist, present no difficulty, and higher eccentricities can also be achieved, with the proviso that l_{\max} may need to be increased, which would lengthen computation times.

ACKNOWLEDGMENTS

We thank the referee for a careful read of the manuscript. This work was supported by NSF grant AST/1108977.

REFERENCES

- Avriël M., 1976, *Nonlinear Programming – Analysis and Methods* (Prentice-Hall, Englewood Cliffs NJ)
- Bailin J. & Steinmetz M., 2005, *ApJ* 627, 647
- Bender R. & Möllenhof C., 1977, *A&A* 177, 71
- Binney J. & Tremaine S., 2008, *Galactic Dynamics* (Princeton University Press, Princeton NJ)
- Bullock J. S., Dekel A., Kolatt T. S., Kravtsov A. V., Klypin A. A., Porciani C. & Primack J. R., 2001, *ApJ* 555, 240
- Capuzzo-Dolcetta R., Leccesse L., Merritt D., Vicari A., 2007, *ApJ* 666, 165
- Cardone V. F., Piedipalumbo E. & Tortora C., 2005, *MNRAS* 358, 1325
- Chanamé, J., Kleyna, J., van der Marel, R. 2008, *ApJ* 682, 841
- Cole S. & Lacey C., 1996, *MNRAS* 281, 716
- Das P., Gerhard O., Mendez R. H., Teodorescu, A. M. & de Lorenzi F., 2011, *MNRAS*, 415, 1244
- Debattista V. P., Moore B., Quinn T., et al. 2008, *ApJ* 681, 1076
- Dehnen W., 2009, *MNRAS* 395, 1079 (D09)
- De Lorenzi F., Debattista V. P., Gerhard O. & Sambhus N., 2007, *MNRAS* 376, 71 (DL07)
- De Lorenzi F., Gerhard O., Saglia R. P., Sambhus, N., Debattista V. P., Pannella M. & Mendez R. H., 2008, *MNRAS* 385, 1729
- De Lorenzi F., Gerhard O., Coccatto L, et al. 2009, *MNRAS* 395, 76
- de Zeeuw T. & Lynden-Bell D., 1985, *MNRAS* 215, 713
- de Zeeuw T., 1985 *MNRAS* 216, 273
- Diemand J., Moore B. & Stadel J., 2004, *MNRAS* 353, 624
- Diemand J., Zemp, M., Moore B., Stadel J. & Carollo C. M., 2005, *MNRAS* 364, 665
- Diemand J. & Moore B., 2011, *ASL* 4, 297
- Dubinski J. & Carlberg R. G., 1991, *ApJ* 378, 496
- Einasto J. & Haud U., 1989, *A&A* 223, 89
- Frenk C. S., White, S. D. M., Davis M. & Efstathiou G., 1988, *ApJ* 327, 507
- Frenk C. S. & White S. D. M., 2012, *AnP* 524, 507
- Fukushige T. & Makino J., 2001, *ApJ* 557, 533
- Gao L., et al., 2008 *MNRAS* 387, 536
- Gerhard O., 2010, *HiA*, 15, 198G
- Hansen S. H., 2009, *ApJ*, 694, 1250
- Holley-Bockelmann K., Mihos J. C., Sigurdsson, S., & Hernquist L., 2001, *ApJ* 549, 862
- Hunt J. A. S. & Kawata D., 2013, *MNRAS*, 430, 1928
- Jing Y. P. & Suto Y., 2002, *ApJ* 574, 538 (JS02)
- Katz N., 1991, *ApJ* 368, 325
- Long R. J. & Mao S., 2010, *MNRAS* 405, 301
- Long R. J. & Mao S., 2012, *MNRAS* 425, 2580
- Long R. J., Mao S., Shen J. & Wang Y., 2013, *MNRAS*,

- 248, 3478
- Ludlow A. D., Navarro J. F., Boylan-Kolchin M., Springel V., Jenkins A., Frenk C. S. & White S. D. M., 2011, MNRAS 415, 3895
- May A. & Binney J., 1986, MNRAS 221, 13
- Merritt D., 1997, ApJ 486, 102
- Merritt D. & Fridman T., 1996, ApJ 460, 136
- Merritt D., Navarro J. F., Ludlow A. & Jenkins A., 2005, ApJ 624, L85
- Merritt D., Graham A. W., Moore B., Diemand J. & Terzić B., 2006 AJ, 132, 2685
- Moore B., Quinn, T., Governato, F., Stadel, J. & Lake, G., 1999, MNRAS 310, 1147
- Moore B., Kazantzidis S., Diemand J. & Stadel J., 2004, MNRAS 354, 522
- Morganti L. & Gerhart O., 2012, MNRAS, 422, 1571
- Navarro J. F., Frenk C. S. & White S. D. M., 1996, ApJ 462, 563 (NFW)
- Navarro J. F., Hayashi E., Power C., et al. 2004, MNRAS 349, 1039
- Navarro J. F., Ludlow A., Springel V., et al. 2010, MNRAS 402, 21
- Power C., Navarro J. F., Jenkins A., et al. 2003, MNRAS 338, 14
- Richstone, D.O. & Tremaine S., 1988, ApJ 327, 82
- Rodionov S. A. & Sotnikova N. Ya., 2006, AR 50, 983
- Rodionov S. A., Athanassoula E. & Sotnikova N. Ya., 2009, MNRAS 392, 904
- Schneider M. D., Frenk C. S. & Cole S., 2012, JCAP 5, 30 (arXiv:1111.5616) (SFC12)
- Schwarzschild M., 1979, ApJ 232, 236
- Schwarzschild M., 1993, ApJ 409, 563
- Sellwood J. A., 2003, ApJ 587, 638
- Sellwood J. A., 2008, ApJ 679, 379
- Sellwood J. A., 2014, arXiv:1406.6606
- Sellwood J. A. & Debattista V. P., 2009, MNRAS 398, 1279
- Springel V., Wang J., Vogelsberger M., et al. 2008, MNRAS 391, 1685
- Syer D. & Tremaine S., 1996, MNRAS 282, 223 (ST96)
- Udry S. & Pfenniger D., 1988, A&A 198, 135
- Valluri M. & Merritt D., 1998, ApJ 506, 686
- Valluri M., Debattista V. P., Quinn T. & Moore B., 2010, MNRAS 403, 525
- van de Ven G., de Zeeuw P. T., van den Bosch, R. C. E., 2008, MNRAS 385, 614
- Vasiliev E. & Athanassoula E., 2012, MNRAS 419, 3268
- Widrow L., 2008, ApJ 679, 1232
- Wojtak R., Lokas E. L., Gottlöber S. & Mamon G. A., 2005, MNRAS 361L, 1
- Zemp, M., 2009, MPLA 24, 2291 (arXiv:astro-ph/0909.4298)

